

From Rayleigh-Bénard convection to porous-media convection: how porosity affects heat transfer and flow structure

Shuang Liu^{1,2}, Linfeng Jiang¹, Kai Leong Chong³, Xiaojue Zhu⁴,
Zhen-Hua Wan⁵, Roberto Verzicco^{6,7,3}, Richard J. A. M. Stevens³,
Detlef Lohse^{3,8}, Chao Sun^{1,2} †

¹Center for Combustion Energy, Key Laboratory for Thermal Science and Power Engineering of Ministry of Education, International Joint Laboratory on Low Carbon Clean Energy Innovation, Department of Energy and Power Engineering, Tsinghua University, Beijing 100084, China

² Department of Engineering Mechanics, School of Aerospace Engineering, Tsinghua University, Beijing 100084, China

³Physics of Fluids Group and Max Planck Center Twente, University of Twente, PO Box 217, 7500AE Enschede, The Netherlands

⁴Center of Mathematical Sciences and Applications, and School of Engineering and Applied Sciences, Harvard University, Cambridge, MA 02138, USA

⁵Department of Modern Mechanics, University of Science and Technology of China, Hefei, Anhui 230027, China

⁶Dipartimento di Ingegneria Industriale, University of Rome ‘Tor Vergata’, Via del Politecnico 1, 00133 Roma, Italy

⁷Gran Sasso Science Institute - Viale F. Crispi, 7, 67100 LAquila, Italy

⁸Max Planck Institute for Dynamics and Self-Organization, 37077 Göttingen, Germany

(Received xx; revised xx; accepted xx)

We perform a numerical study of the heat transfer and flow structure of Rayleigh-Bénard (RB) convection in (in most cases regular) porous media, which are comprised of circular, solid obstacles located on a square lattice. This study is focused on the role of porosity ϕ in the flow properties during the transition process from the traditional RB convection with $\phi = 1$ (so no obstacles included) to Darcy-type porous-media convection with ϕ approaching 0. Simulations are carried out in a cell with unity aspect ratio, for the Rayleigh number Ra from 10^5 to 10^{10} and varying porosities ϕ , at a fixed Prandtl number $Pr = 4.3$, and we restrict ourselves to the two dimensional case. For fixed Ra , the Nusselt number Nu is found to vary non-monotonously as a function of ϕ ; namely, with decreasing ϕ , it first increases, before it decreases for ϕ approaching 0. The non-monotonous behaviour of $Nu(\phi)$ originates from two competing effects of the porous structure on the heat transfer. On the one hand, the flow coherence is enhanced in the porous media, which is beneficial for the heat transfer. On the other hand, the convection is slowed down by the enhanced resistance due to the porous structure, leading to heat transfer reduction. For fixed ϕ , depending on Ra , two different heat transfer regimes are identified, with different effective power-law behaviours of Nu vs Ra , namely, a steep one for low Ra when viscosity dominates, and the standard classical one for large Ra . The scaling crossover occurs when the thermal boundary layer thickness and the pore scale are comparable. The influences of the porous structure on the temperature and velocity fluctuations, convective heat flux, and energy dissipation rates are analysed,

† Email address for correspondence: chaosun@tsinghua.edu.cn

further demonstrating the competing effects of the porous structure to enhance or reduce the heat transfer.

Key words: Turbulent convection, convection in porous media

1. Introduction

Thermal convection is an omnipresent phenomenon in nature and technology. One of the paradigms for thermal convection studies is Rayleigh-Bénard (RB) convection, i.e., convection in a container heated from below and cooled from above, and it has been studied extensively over the last few decades (Ahlers *et al.* 2009; Lohse & Xia 2010; Chillà & Schumacher 2012; Xia 2013). Also the related problem of convection in a fluid-saturated porous medium has received increasing attention owing to its importance in a wide range of natural and industrial processes, such as geothermal energy recovery and geological sequestration of carbon dioxide (Cinar *et al.* 2009; Hassanzadeh *et al.* 2007; Orr 2009; Huppert & Neufeld 2014; Riaz & Cinar 2014; Cinar & Riaz 2014; Emami-Meybodi & Hassanzadeh 2015; De Paoli *et al.* 2016; Soltanian *et al.* 2016; Amooie *et al.* 2018). It is indeed of both fundamental and practical interest to study RB convection in porous media, and considerable progress has been achieved over the years based on the combinations of experimental, numerical, and theoretical studies (Lapwood 1948; Wooding 1957; Joseph *et al.* 1982; Otero *et al.* 2004; Nield & Bejan 2006; Araújo *et al.* 2006; Landman & Schotting 2007; Hewitt *et al.* 2012, 2014; Wen *et al.* 2015; Keene & Goldstein 2015; Ataei-Dadavi *et al.* 2019; Chakkingal *et al.* 2019).

For pure RB convection, in particular, the heat transfer and flow structure have been studied extensively (Ahlers *et al.* 2009). There also has been rapid progress in the modelling of RB convection with additional effects, such as multiphase RB convection (Lakkaraju *et al.* 2013; Wang *et al.* 2019), convection with rough walls (Shishkina & Wagner 2011; Wagner & Shishkina 2015; Zhu *et al.* 2017; Jiang *et al.* 2018; Zhu *et al.* 2019), tilted convection (Shishkina & Horn 2016; Zwirner & Shishkina 2018; Wang *et al.* 2018; Jiang *et al.* 2019), and partitioned RB convection (Bao *et al.* 2015). In the numerical study of confined inclined RB convection in low-Prandtl-number fluids, Zwirner & Shishkina (2018) identified significant heat transfer enhancement, which is closely related to the organization of the plumes in inclined convection, namely, the formation of system-sized plume columns impinging on the opposite boundary layers. Also porous-media convection can be understood as geometrically modified RB convection, with correspondingly modified heat transfer and flow structure. In this study we want to investigate how these flow properties are affected by the porous structure.

When a porous medium is present in a convection cell, the convection is blocked and the flow is stabilized. For given strength of the driving buoyancy force, the strength of the stabilizing effect can be quantified by the porosity. The stabilizing effect is stronger for greater blockage, i.e., for smaller porosity ϕ . However, the interplay between stabilizing and driving forces can result in surprising effects. Examples include confined RB convection (Chong *et al.* 2015, 2018), rotating RB convection (Zhong *et al.* 2009; Stevens *et al.* 2009), and double diffusive convection (Yang *et al.* 2015, 2016). Chong *et al.* (2017) compared these three cases and found that in all three cases, the appropriate strength of the stabilizing force leads to significant heat transfer enhancement due to increased flow coherence, in particular, revealing a universal mechanism of the turbulent transport

enhancement in the presence of stabilizing forces. Obviously, when the stabilizing force becomes even stronger, the flow motion is eventually suppressed, leading to heat transfer reduction. Consequently, the heat transport varies non-monotonously with the strength of the stabilizing force. Also from this comparative perspective between the different systems, it is of interest to investigate how the stabilizing effect of a porous structure affects the heat transfer and flow structure of RB convection.

For modelling porous-media convection, various studies have been conducted focusing on the Darcy-type convection. Related numerical simulations are generally performed based on coarse-grained macroscopic models, such as Darcy's law and its extensions (Otero *et al.* 2004; Hewitt *et al.* 2012, 2014; Wen *et al.* 2015). In these macroscopic models, it is assumed that a macroscopic index, the permeability, relates the average fluid velocity through the pores to the pressure drop.

Recently, the numerical study of Darcy convection has been extended to very high Rayleigh numbers and the linear classical scaling for the Nusselt number with respect to the so-called Darcy Rayleigh number $Ra^* = RaDa$ has been observed (Hewitt *et al.* 2012, 2014). (All these dimensionless numbers are exactly defined later in the paper.) Studies of non-Darcy porous-media convection commonly address the extension of the Darcy regime, such as the inclusion of the inertial effect (Nield & Bejan 2006). Nithiarasu *et al.* (1997) developed a coarse-grained, generalized model of non-Darcy convection, which yields the single-phase model in the limit of unity porosity. Based on this model, they found that in the Darcy regime Nu is determined by the Darcy Rayleigh number Ra^* and is independent of the individual values of the Rayleigh number Ra and Darcy number Da . In contrast, in the non-Darcy flow regime, Nu is significantly affected by both the Rayleigh number and the Darcy number, and by the porosity.

Although both the traditional RB convection without a porous structure and the Darcy-type porous-media convection have been studied extensively, fewer studies have been done to reveal the physics of the transition process between these two extreme cases. One of the few studies focuses on the effect of the buoyancy strength on the flow properties of RB convection in specified porous media (Keene & Goldstein 2015). That study involved experimental measurements of heat transfer properties of RB convection in a cubic enclosure containing a packed bed of spheres, and it was found that the heat transfer properties at high Rayleigh numbers approach the behaviour of a homogeneous fluid layer without spheres. Ataei-Dadavi *et al.* (2019) performed an experimental study of RB convection in an enclosure, filled with solid packing of relatively large spheres. The influences of the packing type, size, and conductivity of the spheres on the flow and heat transfer were investigated for varying Rayleigh numbers, and two heat transfer regimes were observed. One is a reduced heat transfer regime at lower Rayleigh numbers, and the other one is the asymptotic regime at high Rayleigh numbers, where the Nusselt number lines up with the results of the traditional RB convection without spheres.

In related work, Chakkingal *et al.* (2019) carried out numerical simulations of RB convection in a cubic cell packed with relatively large solid spheres and identified three different flow regimes depending on the solid-to-fluid thermal conductivity and Rayleigh number. At low Rayleigh numbers, the convective heat transfer is effectively suppressed, whereas the overall heat transfer can be enhanced for high-conductivity packings due to the significant contribution of the conductive heat transfer. At intermediate Rayleigh numbers, the convective flow is highly suppressed for the high-conductivity packing case, due to the strongly stabilizing effect of the packing on the stratified temperature distribution. The total heat transfer is then lower than that in the classical RB convection case. At higher Rayleigh numbers, convection is the dominant mechanism of heat transfer and then the convective heat transfer is close to that of classical RB convection.

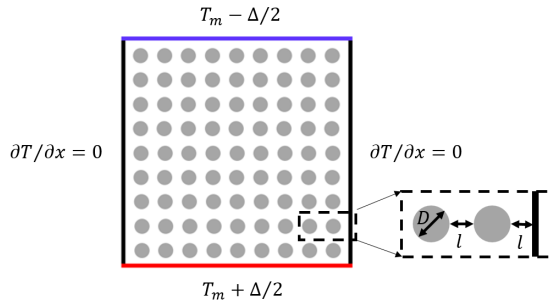


FIGURE 1. Schematic configuration of the RB convection in regular porous media.

Despite all of these studies, the nature of the transition between the traditional RB convection and Darcy-type porous-media convection is still not well understood, and further studies are required to investigate the effects of the porosity on the heat transfer and flow structure. Detailed examinations of microscale flow field are needed to gain a comprehensive understanding of this transition process and its underlying physical mechanism.

In this study we perform a numerical investigation of a representative porous medium model, namely two-dimensional (2D) RB convection in regular porous media, trying to gain an understanding of the transition process between the two distinct convection regimes. A schematic of the flow configuration is shown in figure 1. Circular, solid obstacles are spaced uniformly on a square lattice. In such a pore-scale model, the detailed flow in the pores is resolved and the interaction between the porous medium and various flow structures of convection is faithfully captured, which are essential to connect the macroscopic properties with the microscale mechanisms.

The heat transfer properties and flow structures of the porous-media convection are investigated for varying Rayleigh numbers Ra and porosities ϕ , at a fixed Prandtl number $Pr = 4.3$. Figure 2 shows the effect of the porosity ϕ on the heat transfer (in its dimensionless form, the Nusselt number Nu) for $Ra = 10^7$ and 10^8 . It is observed that $Nu(\phi)$ varies non-monotonously as ϕ is decreased from 1 (so no obstacles included). First, when ϕ is slightly decreased, the heat transfer is enhanced, and then when ϕ is sufficiently small, it is reduced as compared to the $\phi = 1$ case. Correspondingly, there is an optimum porosity for the heat transfer, which depends on Ra . The non-monotonic behaviour of $Nu(\phi)$ is reminiscent of the influence of other stabilizing force on turbulent transport through coherent structure manipulation (Chong *et al.* 2017), which we discussed above.

The objective of this study is to further understand this non-monotonic behaviour of $Nu(\phi)$ and to clarify the connection of this system to other stabilizing-destabilizing flows. In particular, we will reveal how the porous structure induces the two competing effects on the heat transfer and how they depend on the Rayleigh number and on the porosity ϕ , and will connect the observed global transport properties to the local energy dissipation rates.

Although the real physical system is three-dimensional (3D), we employ the 2D configuration, as we want to reveal the dominant effects of porous media over a wide range of parameters, for which 3D simulations are still prohibitive. Moreover, as the 2D numerical simulations are computationally less demanding, a sufficient flow resolution can be guaranteed. In a detailed examination of the differences and similarities between two- and three-dimensional RB convection, van der Poel *et al.* (2013) found that for a large range of Ra and large $Pr > 1$, the Nu vs Ra scaling behaviours in two- and three-dimensional convection are comparable up to constant prefactors, which justifies our

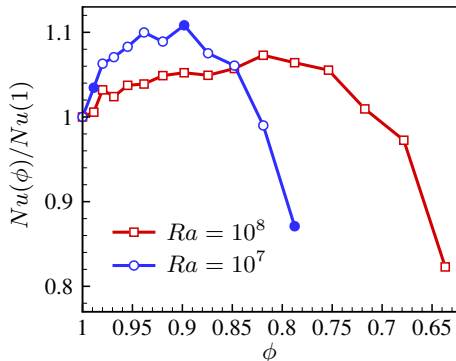


FIGURE 2. Normalized Nusselt number $Nu(\phi)/Nu(1)$ at $Ra = 10^7$ and 10^8 . Snapshots of the instantaneous temperature field corresponding to the filled symbols will be shown in figure 8.

2D simulation at $Pr = 4.3$ chosen by us (corresponding to water) for the traditional RB convection without obstacles. The phenomena observed in the 2D problem with obstacles may also be relevant to the 3D case. The investigation of 3D cases will be the focus of a subsequent study.

The remainder of this paper is organized as follows. The numerical model is described in detail in §2, including the governing equations of the pore-scale simulations and the numerical methods. We present the main results in §3, §4, and §5, focusing on the heat transfer properties, the flow structures, and the energy dissipation rates, respectively. In §6 we will summarize our findings and give an outlook on further work.

2. Numerical model

2.1. Governing equations

We consider a Boussinesq fluid in a 2D RB cell with unity aspect ratio, containing an obstacle array located on a square lattice, as depicted in figure 1. The fluid is heated from below and cooled from above with a temperature difference Δ between two horizontal plates a distance L apart in the vertical direction. The diameter of the circular, solid obstacles is D . The minimum value of the obstacle-obstacle and obstacle-wall separations is l . The porous structures are characterized by the porosity ϕ , which measures the volume fraction of the fluid phase. A value of $\phi = 1$ corresponds to the traditional RB convection without the obstacle array. For the convection cell with unity aspect ratio, we have $l = (L - N \times D)/(N + 1)$, where N is the number of the obstacles along the horizontal and vertical directions. The corresponding porosity is $\phi = 1 - N^2\pi D^2/(4L^2)$. For fixed D , only specific values of ϕ (or l) can be achieved, since N is an integer. We note that, besides the case with regular obstacle arrangement on a square lattice, the effect of obstacle arrangement will also be considered in this study (see figure 11). The non-dimensional governing equations describing the flow dynamics in the pores read

$$\begin{aligned}
 \frac{\partial \vec{u}}{\partial t} + \vec{u} \cdot \nabla \vec{u} &= -\nabla p + \sqrt{\frac{Pr}{Ra}} \nabla^2 \vec{u} + T \vec{e}_z + \vec{f}, \\
 \frac{\partial T}{\partial t} + \nabla \cdot (\vec{u} T) &= \frac{1}{\sqrt{Pr Ra}} \nabla^2 T, \\
 \nabla \cdot \vec{u} &= 0,
 \end{aligned} \tag{2.1}$$

where \vec{u} is the velocity vector with components (u, v) along the horizontal and vertical directions (x, z) , p is the pressure, T is the temperature and \vec{e}_z is the unit vector in the vertical direction. The immersed boundary force term \vec{f} is added to account for the presence of the obstacle array. The governing equations were non-dimensionalized using L for length, Δ for temperature, the free-fall velocity $U = \sqrt{g\beta\Delta L}$ for velocity and L/U for time, where g is the gravitational acceleration and β the isobaric expansion coefficient.

The two dimensionless parameters in the governing equations (2.1) are the Rayleigh number, $Ra = g\beta\Delta L^3/(\nu\kappa)$, and the Prandtl number, $Pr = \nu/\kappa$, where ν is the kinematic viscosity and κ the thermal diffusivity. The heat transfer property is measured by the Nusselt number, $Nu = \sqrt{RaPr}\langle vT \rangle_{x,t} - \langle \partial_z T \rangle_{x,t}$, where $\langle \cdot \rangle_{x,t}$ denotes taking averages over any horizontal plane and time. In practice, the average is taken over the top and bottom plates. No-slip and no-penetration boundary conditions are imposed at all solid surfaces, including the fluid-obstacle interfaces. The horizontal top and bottom plates are isothermal and the sidewalls are thermally insulated.

Note that the heat transfer between the fluid and solid phases is considered. For simplicity, we assume the same thermal properties for the two phases, including ρc_p , thermal conductivity k , and thermal diffusivity $\kappa = k/(\rho c_p)$, where ρ is the density and c_p the specific heat capacity. The temperature equation for the fluid and solid phases reads

$$\frac{\partial T}{\partial t} + \nabla \cdot (\vec{u}_{cp} T) = \frac{1}{\sqrt{PrRa}} \nabla^2 T, \quad (2.2)$$

where \vec{u}_{cp} (to be defined below) is the velocity for the fluid and solid phases depending on the position in the domain (Verzicco 2002, 2004; Stevens *et al.* 2014; Ardekani *et al.* 2018a,b; Sardina *et al.* 2018).

2.2. Numerical methods

In this subsection the essential elements of the numerical methods are presented. The governing equations are discretized using a second-order finite-difference method with a pressure-correction scheme. A fractional-step third-order Runge-Kutta scheme is employed for the time stepping of the explicit terms and a Crank-Nicholson scheme for the implicit terms. A uniform, staggered, Cartesian grid is used in this study. The pressure Poisson equation is solved efficiently using a FFT-based solver. For more details of the numerical schemes of the governing equations, we refer the reader to van der Poel *et al.* (2015).

To account for the obstacle array, a direct-forcing immersed boundary method (IBM) in the Euler-Lagrange framework is adopted (Uhlmann 2005; Breugnot 2012). For the resolution of the obstacles, N_L markers are distributed uniformly along the boundary of each obstacle, with the Lagrangian grid size being about 0.7 times of the Eulerian grid size. In each Runge-Kutta substep, a first prediction velocity is obtained by advancing the momentum equations in time without considering the IBM force \vec{f} . The first prediction velocity is then interpolated from the Eulerian grid to the Lagrangian grid using the moving-least-squares approach (Vanella & Balaras 2009; de Tullio & Pascazio 2016; Spandan *et al.* 2017, 2018). The IBM force \vec{f} required on each Lagrangian marker for satisfying no-slip and no-penetration conditions is computed, which is then spread back to the Eulerian grid using the moving-least-squares approach. The force \vec{f} is used to update the velocity, followed by a standard pressure correction step. We note that the pressure field required to enforce the incompressibility condition has vanishing gradient at the immersed boundary. Thus, the pressure correction step does not change practically the numerical accuracy of the IBM scheme, as observed by Fadlun *et al.* (2000) and Kempe

TABLE 1. Numerical details of the typical grid resolutions. The columns from left to right denote the Rayleigh number Ra , the number of obstacles N_o , the porosity ϕ , the grid resolution $N_x \times N_z$, the Nusselt number Nu , the number of grid nodes N_{BL} in the thermal boundary layers, and the number of grid nodes N_D per obstacle diameter. The thickness of thermal boundary layer is estimated as $\delta_{th} = L/(2Nu)$. We note that the table only presents some typical cases. Totally, 67 different cases were simulated, and the results are collected in figure 3.

Ra	N_o	ϕ	$N_x \times N_z$	Nu	N_{BL}	N_D
10^6	144	0.82	540×540	2.77	97	22
10^7	144	0.82	540×540	12.89	21	22
10^8	144	0.82	540×540	28.16	10	24
10^9	144	0.82	1080×1080	53.40	10	43
10^{10}	144	0.82	3072×3072	106.1	14	123

& Fröhlich (2012). As a validation of the implementation of the IBM, we considered a steady, axisymmetric shear flow inside a circular domain driven by the rotation of the circular boundary at a fixed rotation rate without body force. The numerical simulation showed that the azimuthal velocity increases linearly with the distance away from the rotation axis and the vorticity is uniform, in quantitative agreement with the theoretical results.

The heat transfer between the fluid and solid phases is realized by solving the temperature equation (2.2) in both phases (Ardekani *et al.* 2018a,b; Sardina *et al.* 2018). A phase indicator ξ is introduced to represent the solid volume fraction and to distinguish the fluid and solid phases on each grid point of two components of velocity. The value of ξ is determined from a level-set function ζ given by the signed distance of four corner nodes to the obstacle surface using the formula (Ardekani *et al.* 2018a; Kempe & Fröhlich 2012)

$$\xi = \frac{\sum_{n=1}^4 -\zeta_n \mathcal{H}(-\zeta_n)}{\sum_{n=1}^4 |\zeta_n|}, \quad (2.3)$$

where \mathcal{H} is the Heaviside step function. Then the velocity of the combined phase is defined at each point in the computational domain as

$$\vec{u}_{cp} = (1 - \xi)\vec{u}_f + \xi\vec{u}_p, \quad (2.4)$$

where \vec{u}_f and \vec{u}_p denote velocities of the fluid and solid phases, respectively. For fixed obstacles considered in this study we obviously have $\vec{u}_p = 0$. We note that the coupling of the IBM and heat transfer between different phases has been considered in other convection problems, such as the turbulent convection confined by walls with finite conductivities (Verzicco 2002, 2004; Stevens *et al.* 2014).

In this study a uniform Eulerian grid is used and the resolution is chosen to fully resolve the boundary layers and the smallest scales in the bulk (Stevens *et al.* 2010; Shishkina *et al.* 2010; Zhang *et al.* 2017). The numerical details of some typical grid resolutions are given in table 1. For the small- Ra cases, the grid is restricted by the resolution of the obstacles. For these cases a grid of 540×540 is used, and the number of grid nodes per obstacle diameter is 22. For larger Ra , the mesh size chosen is adequate to achieve a full resolution of the thermal boundary layer, with the thermal boundary layer resolved by at least 10 grid points. For the highest Ra ($Ra = 10^{10}$), a grid of 3072×3072 is used.

This ensures that the turbulent flow in the bulk and boundary layers is fully resolved. For the traditional RB convection at $Ra = 10^{10}$, the typical Kolmogorov length scale η is estimated by the global criterion $\eta = LPr^{1/2}/[Ra(Nu - 1)]^{1/4}$, and the Batchelor scale η_B is estimated by $\eta_B = \eta Pr^{-1/2}$ (Shishkina *et al.* 2010). We find that the grid spacing Δ_g satisfies $\Delta_g \lesssim 0.16\eta$ and $\Delta_g \lesssim 0.33\eta_B$. The thermal boundary layers are resolved with 14 grid points, which agrees with the recommendations of Shishkina *et al.* (2010). Long-time averages are conducted for the calculation of Nu . The difference of Nu obtained by time averages over the first and second halves of the simulations (both taken after initial transients) was smaller than 1%. Besides, the relative difference between the top- and bottom-wall Nu was smaller than 1%.

Simulations were performed for varying Rayleigh numbers (from 10^5 to 10^{10}) and porosities (from 0.75 to 1). The Prandtl number and obstacle diameter were fixed at $Pr = 4.3$ and $D = 0.04$, respectively.

3. Heat transfer

In this section the influence of the obstacle array on the heat transfer properties is examined. The presence of the obstacle array has a significant influence on the heat transfer properties. The normalized Nusselt number $Nu(\phi)$ for two fixed Ra was already shown in figure 2. In figure 3, $Nu(Ra)$ for five fixed porosities ϕ is shown. In the traditional RB convection with $\phi = 1$, Nu increases with Ra following an effective power law $Nu \sim Ra^{0.30}$, consistent with the results in the literature for 2D RB convection (van der Poel *et al.* 2013; Zhu *et al.* 2017; Zhang *et al.* 2017). For fixed $\phi < 1$, it is found that the variation of Nu with Ra exhibits two scaling regimes for the parameter range studied. Compared with the results of traditional RB convection with $\phi = 1$, the heat transfer is reduced for small Ra even if Nu increases with Ra with a steep effective power law $Nu \sim Ra^{0.65}$; on the other hand, for large enough Ra , Nu becomes larger than the corresponding value without obstacles and increases with Ra with an effective power law $Nu \sim Ra^{0.30}$, similar to that of traditional RB convection. The increase of Nu in the large- Ra regime is more visible in the compensated plot of figure 3(b) and in figure 2. Note that the regime of heat transfer enhancement with decreasing ϕ displayed in figure 2 corresponds to the large- Ra regime shown in figure 3. Figure 3(a,b) shows that the trends of variation of Nu with Ra for different values of ϕ are similar, and the critical Ra for scaling crossover increases as ϕ is decreased. Considering that the values of ϕ and Nu determine the characteristic length scales of the regular porous medium and flow structures, respectively, the scaling crossover indicates a competition of the length scale of porosity and that of the flow structures. When we rescale the thermal boundary layer thickness $\delta_{th} = L/(2Nu)$ with the obstacle separation l , it is found that the results for different ϕ approximately collapse, and the scaling crossover occurs when $\delta_{th}/l \approx 1$, as shown in figure 3(c). The data collapse indicates that the heat transfer properties are determined by the length scales of the flow structures and the pore scale of the regular porous medium.

It is interesting to examine the relevance of our results to pure Darcy-type convection. For this, it is instructive to show how Nu varies with the so-called Darcy Rayleigh number $Ra^* = RaDa$, where $Da = K/L^2$ is the Darcy number. Here K is the permeability, which depends on the geometry of the porous media and represents the resistance for the fluid to flow through the porous media. We estimate Da with the porosity ϕ and the obstacle

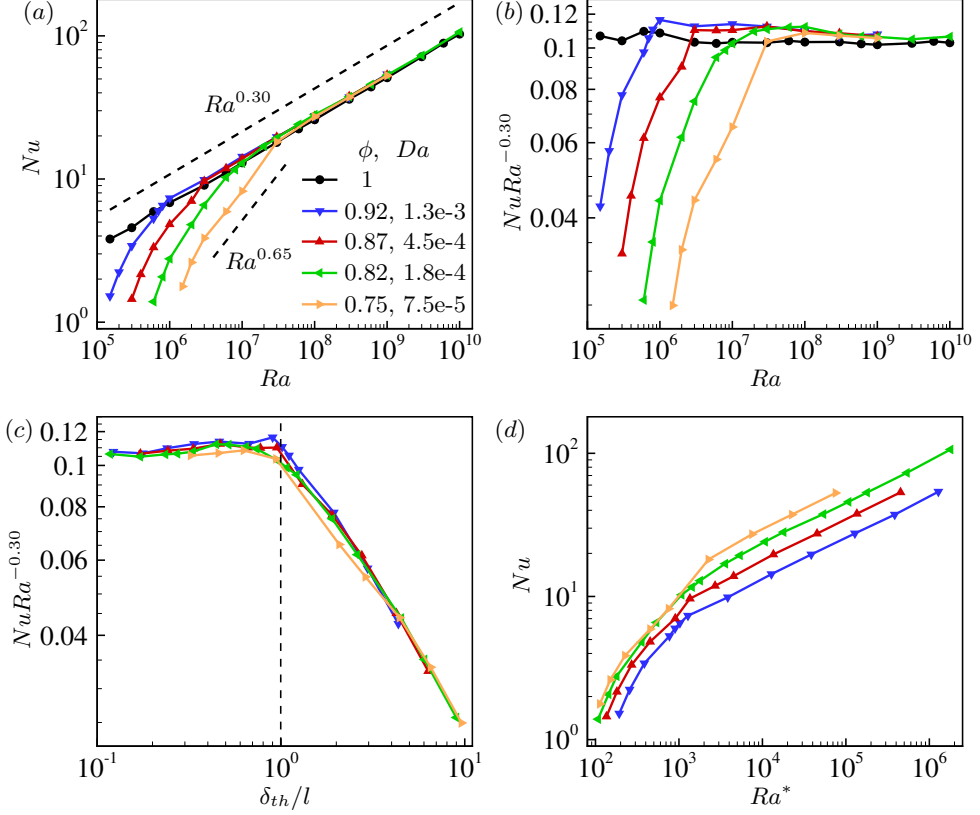


FIGURE 3. (a) Variations of Nu with Ra for different ϕ . (b) The compensated plot of (a). (c) Results for different ϕ collapse by rescaling the thermal boundary layer thickness $\delta_{th} = L/(2Nu)$ with the pore scale l . (d) Variation of Nu with the Darcy Rayleigh number $Ra^* = RaDa$.

diameter D based on the Kozeny's equation (Nithiarasu *et al.* 1997; Nield & Bejan 2006):

$$Da = \frac{\phi^3 D^2}{150(1 - \phi)^2 L^2}. \quad (3.1)$$

The results are shown in figure 3(d). We find that in the small- Ra^* regime, $Nu(Ra^*)$ shows a trend to collapse as ϕ is decreased, which is a signature of the transition to Darcy-type flow and consistent with the observation based on the generalized non-Darcy model (Nithiarasu *et al.* 1997). We note that, in porous media there may exist multiple flow states with different heat transfer efficiencies for the same parameters. The solution may not be able to sample all the flow configurations due to the suppression of fluctuations in the presence of an obstacle array. The numerically realized steady state may be different for different initial conditions. Despite this, we expect that the differences of the statistics of multiple flow states are relatively small, particularly for the large- Ra cases, and the global trend of variation of Nu with Ra and ϕ will not be qualitatively affected by the existence of multiple flow states.

We now focus on the statistics of the velocity and temperature fields on the horizontal mid-plane $z = 0.5$, to quantify the modifications of heat transfer properties as ϕ is decreased, particularly in the regime where $Nu(\phi)$ varies non-monotonously. Figure 4 plots the joint probability density function (PDF) $P(v, \delta T)$ of vertical velocity v and temperature fluctuation δT for different ϕ at $Ra = 10^8$, where $\delta T = T - T_m$ and $T_m = 0.5$

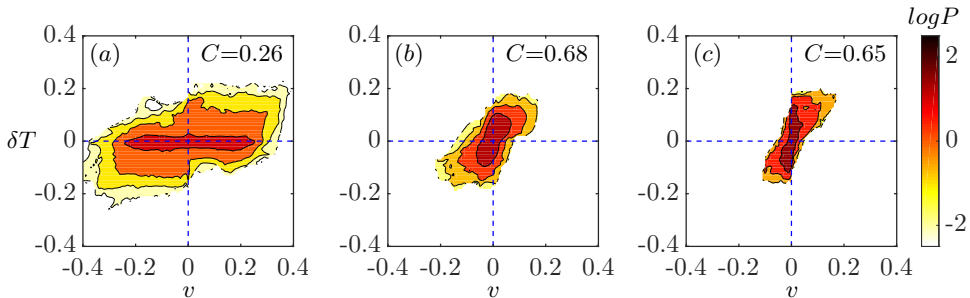


FIGURE 4. The joint PDFs of the vertical velocity v and the temperature fluctuation $\delta T = T - T_m$ on the horizontal mid-plane $z = 0.5$ for different ϕ at $Ra = 10^8$: (a) $\phi = 1$, (b) $\phi = 0.92$, (c) $\phi = 0.82$. Corresponding values of the cross-correlation C between v and δT are labeled at the top right corner of each panel.

is the arithmetic mean temperature. In the absence of the obstacle array (i.e., for $\phi = 1$), the velocity can attain considerably larger values than that in porous media at the same Ra . The temperature in the bulk is well mixed with $\delta T \approx 0$. Thus, $P(v, \delta T)$ is concentrated in a slender region located on the horizontal axis, as shown in figure 4(a). From $P(v, \delta T)$ the correlation between v and δT can be identified. Due to buoyancy, flow elements with positive (negative) δT are more likely to move upward (downward). Note that there is a non-negligible probability for the occurrence of counter-gradient convective heat transfer, which is manifested in the finite values of $P(v, \delta T)$ in the second and fourth quadrants, consistent with the observation of counter-gradient convective heat transfer in Sugiyama *et al.* (2010) and Huang & Zhou (2013). The properties of temperature fluctuations and convective heat transfer can also be quantified by the normalized PDFs of δT and $v \cdot \delta T$ on the horizontal mid-plane $z = 0.5$, which are given in figure 5. The strong mixing of temperature in the bulk is manifested by the peak value of $P(\delta T)$ at $\delta T = 0$ in figure 5(a), and the correlation between v and δT is reflected by the asymmetry of the left- and right-hand branches of $P(v \cdot \delta T)$ in figure 5(b). The counter-gradient convective heat transfer is quantified by the left-hand branch of $P(v \cdot \delta T)$.

As ϕ is decreased, it is found that the fluctuation properties are significantly influenced, as shown in figures 4(b, c). The velocity distribution is narrowed down, showing that the convection strength is decreased for the flow through regular porous media. Compared with the results of traditional RB convection with $\phi = 1$, the temperature mixing is less efficient and large temperature fluctuations are more probable to appear. The decreased mixing efficiency is also manifested by the flattening of the peak of $P(\delta T)$ around $\delta T = 0$ in figure 5(a). From $P(v, \delta T)$ it is found that the counter-gradient convective heat flux is suppressed, which is also manifested by the rapid decrease of the left-hand branch of $P(v \cdot \delta T)$ as $v \cdot \delta T$ is decreased from 0 in figure 5(b). Note that as ϕ is decreased, the distribution of $P(v, \delta T)$ is more compact and concentrated along a line with positive slope, which suggests that the correlation between v and δT is enhanced in regular porous media. We here quantify the correlation between v and δT using the cross-correlation $C \equiv \langle g_v g_T \rangle$, where $g_x \equiv [\chi - \langle \chi \rangle] / \sigma_x$, $\sigma_x \equiv \sqrt{\langle \chi^2 \rangle - \langle \chi \rangle^2}$, and $\langle \cdot \rangle$ denotes the average over the horizontal mid-plane and time. Values of $C = 1$ and -1 correspond to perfect correlations and anti-correlations, respectively, and $C = 0$ corresponds to no correlation. The values of C for the three cases of figure 4 are shown in the top right-hand corner of each panel, which definitely demonstrate the enhancement of the correlation between v and δT with decreasing ϕ . For both the traditional RB convection and convection

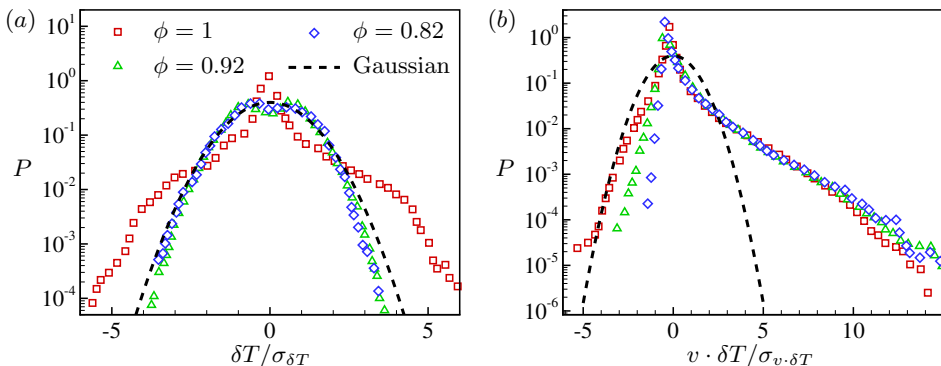


FIGURE 5. The normalized PDFs of (a) $\delta T/\sigma_{\delta T}$ and (b) $v \cdot \delta T/\sigma_{v \cdot \delta T}$ on the horizontal mid-plane $z = 0.5$ for different ϕ at $Ra = 10^8$, where $\sigma_{\delta T}$ and $\sigma_{v \cdot \delta T}$ are the standard deviations of δT and $v \cdot \delta T$, respectively. The dashed lines indicate the Gaussian distribution.

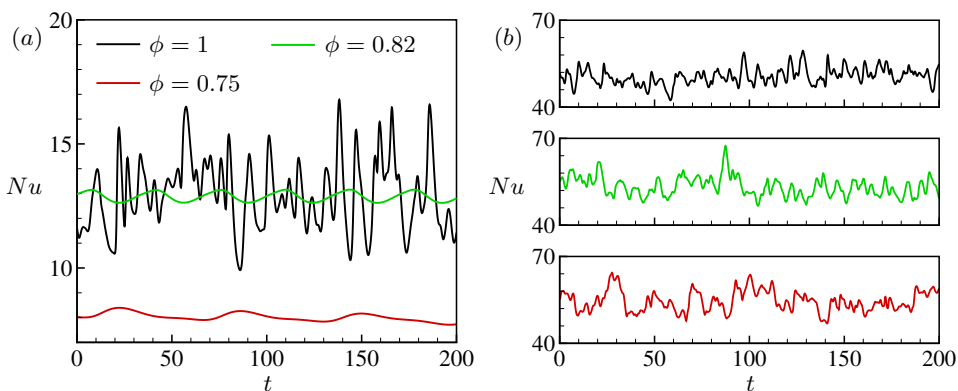


FIGURE 6. Nusselt number $Nu(t)$ in a time interval of 200 dimensionless units for different ϕ at (a) $Ra = 10^7$ and (b) $Ra = 10^9$.

in regular porous media, the cross-correlation between temperature fluctuation δT and horizontal velocity u on the horizontal mid-plane is small with $|C| < 0.1$.

The variation of $P(v, \delta T)$ with ϕ shown in figure 4 leads us to identify two competing effects of the obstacle array on the heat transfer. On the one hand, the flow becomes more coherent with enhanced correlation between temperature fluctuation and vertical velocity. This is beneficial for the heat transfer. On the other hand, the obstacle array slows down the convection due to enhanced resistance, which is unfavorable for the heat transfer. The competing effects of the obstacle array on the heat transfer result in the non-monotonous variation of Nu with ϕ as was already shown in figure 2. As ϕ is slightly decreased from 1, the enhancement of the flow coherence increases the heat transfer efficiency. While when ϕ is small enough, the convection is strongly suppressed, leading to the heat transfer reduction. The heat transfer enhancement by increasing flow coherence is a widespread phenomenon and has been observed in various flow configurations, such as confined RB convection (Huang *et al.* 2013; Chong *et al.* 2018) and partitioned RB convection (Bao *et al.* 2015). Chong *et al.* (2017) revealed a universal, non-monotonous behaviour of turbulent transport in systems with competing stabilizing and destabilizing forces. The non-monotonous variation of Nu with the increase of the stabilizing effect of porous structure is consistent with the observation of Chong *et al.* (2017).

Figure 6 shows sampled time records of Nu for different ϕ at $Ra = 10^7$ and 10^9 , showing the influence of the obstacle array on the temporal characteristics of fluctuations. It is found that for relatively small Ra , the high-frequency fluctuations are significantly suppressed as ϕ is decreased, while for large enough Ra , the suppression of high-frequency fluctuations is less visible for the values of ϕ studied. The influence of the obstacle array on the fluctuations is dependent on the relative magnitudes of the spatial coherence length and the pore scale. At small Ra , the length scales of the flow structures are large compared to the pore scale, and the resistance of the obstacle array to the convection is strong. Thus flow fluctuations are significantly suppressed, and there is no developed turbulence in the pores. As Ra is increased, the convection is more energetic and the length scales of the flow structures are decreased. Thus the obstacle array has smaller effects on the fluctuations, and the flow in the pores becomes chaotic or even turbulent at large enough Ra .

4. Flow structure

In this section we focus on the flow structures of RB convection in regular porous media. Figure 7 displays typical snapshots of the instantaneous temperature T , the velocity magnitude $|\vec{u}|$, and the convective heat flux $v \cdot \delta T$ in the vertical direction. In the traditional RB convection with $\phi = 1$, the flow consists of a well-organized large-scale circulation (LSC) with two well-established counter-rotating corner rolls (Sugiyama *et al.* 2010), as shown in figures 7(a–c). Due to the formation of the LSC, the velocity in the bulk is non-uniform. Following the LSC, plumes detaching from the thermal boundary layers mainly go up and down near the sidewalls. The temperature at the cell center is well mixed with $T \approx T_m$. From the distribution of $v \cdot \delta T$ it is confirmed that counter-gradient convective heat flux appears locally around the LSC and corner rolls, which is due to the bulk dynamics and the competition between the corner-flow rolls and the LSC (Sugiyama *et al.* 2010; Huang & Zhou 2013). The inclusion of an array of obstacles has a significant influence on the flow structures, as displayed in figures 7(d–i). Convection strength is reduced and the LSC is suppressed due to the impedance of the obstacle array. Temperature mixing at the cell center is less efficient. Thermal plumes detaching from the thermal boundary layers can penetrate deep in the bulk, forming convection channels, namely, the regions with strong flows that are formed between the obstacles. When Ra is relatively large, the characteristic length scales of the flow structures are smaller than the pore scale, and the flow is chaotic and dominated by fragmented plumes, as shown in figure 7(d); while when Ra is relatively small the flow is dominated by large-scale plumes, as shown in figure 7(g). Comparing figures 7(f, i) and 7(c), it is found that the counter-gradient convective heat flux is reduced in regular porous media, which is attributed to the suppression of the LSC and coherence of plume dynamics due to the impedance of the obstacle array.

Snapshots of temperature fields at $Ra = 10^7$ and different porosities are shown in figure 8, demonstrating the enhancement of flow coherence with decreasing ϕ . For relatively large ϕ , plumes wander randomly in the bulk, as shown in figure 8(a). As ϕ is further decreased, plumes cannot move freely due to the impedance of the obstacle array and prefer moving along convection channels, as shown in figures 8(b, c).

To further investigate the influence of the obstacle array on the convection, we study the velocity distribution in the bulk region. Figure 9 shows the PDFs of the velocity magnitude $|\vec{u}|$ inside a circular domain of radius r at the cell center for different ϕ at $Ra = 10^8$. In the traditional RB convection with $\phi = 1$, the velocity magnitude is spatially non-uniform due to the formation of the LSC. The mean velocity vanishes at

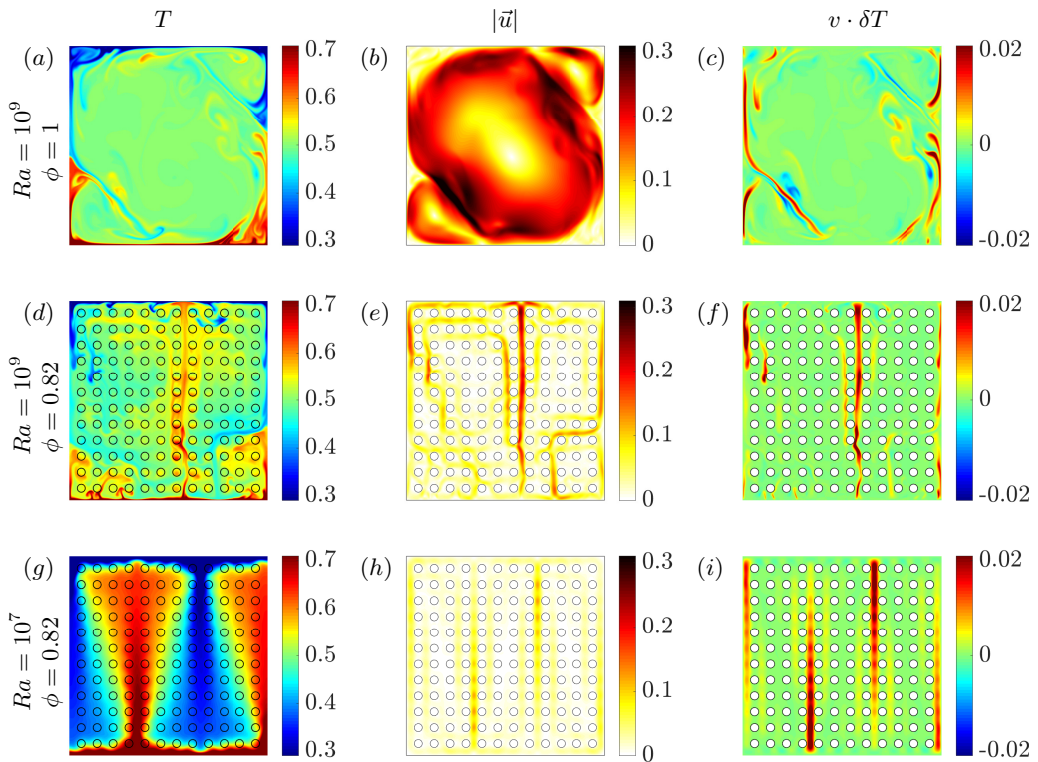


FIGURE 7. Typical snapshots of the instantaneous (a, d, g) temperature T , (b, e, h) the velocity magnitude $|\vec{u}|$, and (c, f, i) the local convective heat flux $v \cdot \delta T$ in the vertical direction at (a, b, c) $(Ra, \phi) = (10^9, 1)$, (d, e, f) $(Ra, \phi) = (10^9, 0.82)$, and (g, h, i) $(Ra, \phi) = (10^7, 0.82)$. Circles in (d – i) indicate the obstacle array. Note that according to the temperature equation (2.2), the temperature in the obstacles is well defined.

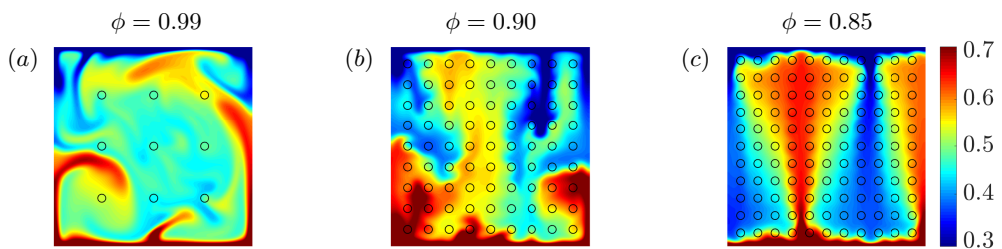


FIGURE 8. Snapshots of the instantaneous temperature field at $Ra = 10^7$ and different ϕ , corresponding to the filled symbols in figure 2: (a) $\phi = 0.99$, (b) $\phi = 0.90$, and (c) $\phi = 0.85$.

the cell center and increases linearly with r at leading order. Due to this non-uniformity, $P(|\vec{u}|)$ shifts along the $|\vec{u}|$ axis as r is increased, and follows a linear relation for small $|\vec{u}|$, $P(|\vec{u}|) \sim |\vec{u}|$, as shown in figure 9(a). The obstacle array has a significant influence on the velocity distribution, as shown in figures 9(b, c). The maximum convection velocity is decreased due to the drag of the obstacle array, and the results for different values of r collapse, indicating that the velocity distribution is spatially uniform in the bulk. The

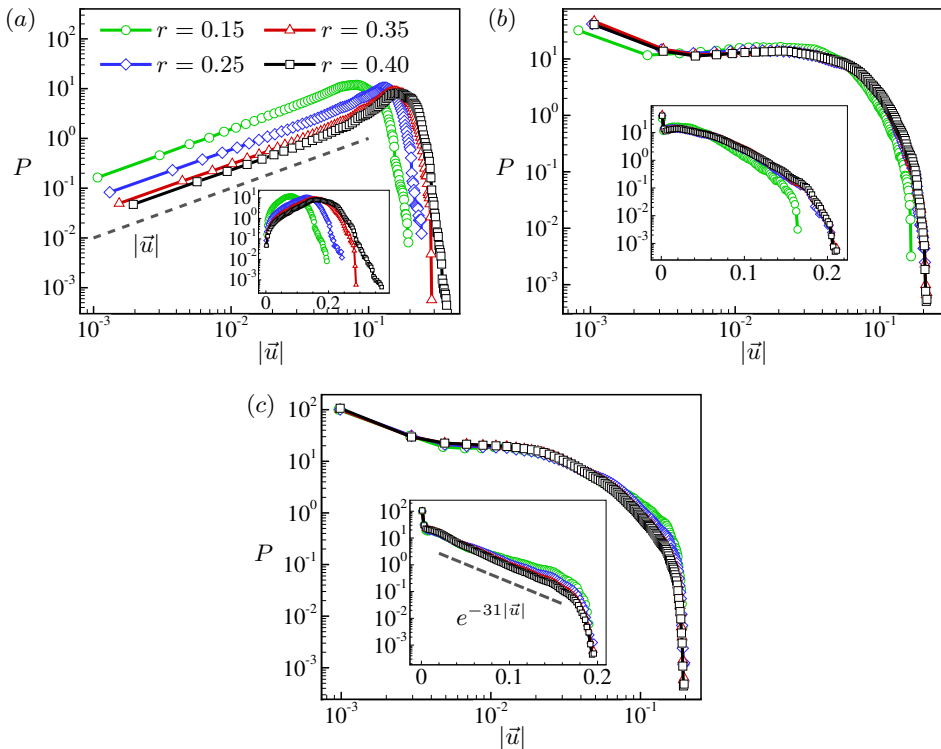


FIGURE 9. Log-log plots of the PDFs of the velocity magnitude $|\vec{u}|$ inside a circular domain of radius r at the cell center for different ϕ at $Ra = 10^8$. (a) $\phi = 1$, (b) $\phi = 0.92$, (c) $\phi = 0.82$. The insets are the same results shown in semi-log plots. In (a) and the inset of (c) guiding lines of constant slope are included, describing the respective scaling behaviours of $P(|\vec{u}|)$. As $|\vec{u}|$ increases, $P(|\vec{u}|)$ increases linearly for small $|\vec{u}|$ in (a), and it decreases exponentially in the intermediate range of $|\vec{u}|$ in (c).

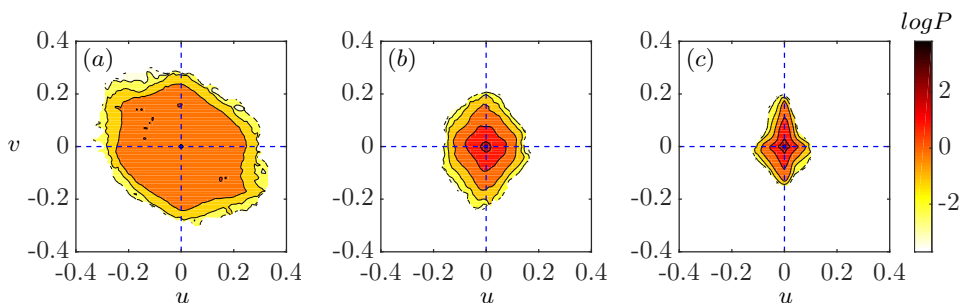


FIGURE 10. The joint PDFs of two velocity components (u, v) inside a circular domain of radius $r = 0.4$ at the cell center for different ϕ at $Ra = 10^8$: (a) $\phi = 1$, (b) $\phi = 0.92$, (c) $\phi = 0.82$.

shape of $P(|\vec{u}|)$ also changes qualitatively and deviates from the power-law distribution as ϕ is decreased. In regular porous media the probability density is larger for $|\vec{u}|$ to take smaller values, and when ϕ is small enough, $P(|\vec{u}|)$ satisfies an exponential distribution, as shown in figure 9(c). The change of velocity distribution demonstrates the transition of flow organization as ϕ is decreased, from the formation of the LSC in the traditional

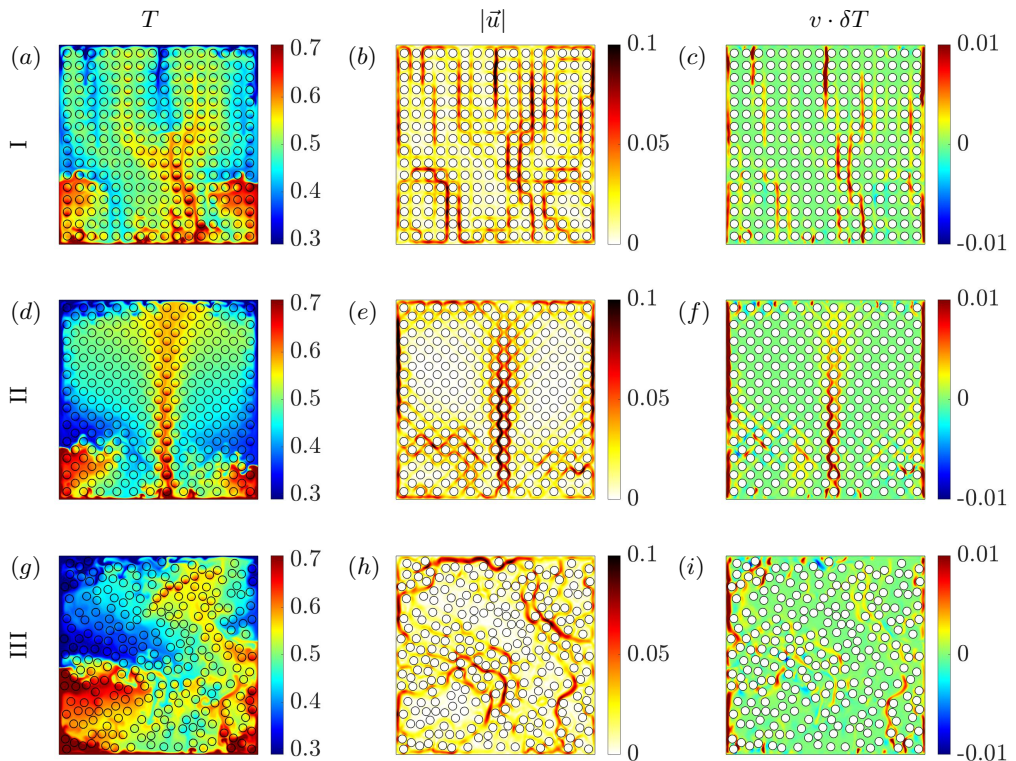


FIGURE 11. Snapshots of (a, d, g) temperature T , (b, e, h) velocity magnitude $|\vec{u}|$, and (c, f, i) the convective heat flux $v \cdot \delta T$ in the vertical direction for three different obstacle arrangements with similar porosities at $Ra = 10^9$. (a, b, c) Porous medium I consists of obstacles located on a square lattice, and the porosity $\phi = 0.68$. (d, e, f) Porous medium II is constructed by rotating the obstacle lattice of I by 45 degrees, with porosity $\phi = 0.67$. (g, h, i) Porous medium III is constructed by randomly placing the obstacles in the cell, with porosity $\phi = 0.68$.

RB convection to the wandering motion of plumes penetrating in the pores in the porous-media convection.

Figure 10 shows the joint PDFs of two velocity components (u, v) inside a circular domain of radius $r = 0.4$ at the cell center for different ϕ at $Ra = 10^8$. It is found that both the size and shape of $P(u, v)$ change as ϕ is decreased from 1. The shrinking of $P(u, v)$ indicates the reduction of convection strength. The change of contour levels manifests the increased probability for $|\vec{u}|$ to take smaller values. When ϕ is small enough, the contour lines of $P(u, v)$ protrude along the horizontal and vertical coordinate axes, indicating the formation of convection channels.

How robust are our results with respect to the arrangement of the obstacles? To answer this question, we study how the obstacle arrangement influences the flow structure. We consider three different arrangements with similar porosities, i.e. two regular arrangements and one random arrangement. Simulations are performed at $Ra = 10^9$. The snapshots of temperature T , velocity magnitude $|\vec{u}|$, and the convective heat flux $v \cdot \delta T$ in the vertical direction are shown in figure 11. It is seen that the flow structure is significantly influenced by the obstacle arrangement. In figures 11(a, b, c), the porous medium I is constructed by placing the circular obstacles on a square lattice, as done in the rest of this paper. As already discussed, thermal plumes can penetrate up and

down without obstruction, forming vertical convection channels with strong fluid and heat transport. In figures 11(*d, e, f*), the regular porous medium II is constructed by rotating the lattice of porous medium I by 45 degrees. In such an obstacle arrangement, the vertical convection channels observed in porous medium I are obstructed by the obstacles, except the vertical channels close to the sidewalls. Despite that, we find that thermal plumes can penetrate deep into the bulk along zigzag channels aligning vertically. Besides, strong fluid and heat transport occur close to the sidewalls, where the fluid can penetrate up and down without obstruction. In figures 11(*g, h, i*), a random porous medium is constructed (porous medium III), with the pore scale $l \geq l_{min} = 0.005$, where l_{min} is the minimum pore scale. It is observed that the plume motion is less organized compared to those in the regular porous media I and II. Curved convection channels with strong flow emerge in the pores, with no preferred flowing directions. Except the localized vertical channels, the curved convection channels are less efficient at transporting heat in the vertical direction. The Nusselt numbers for the obstacle arrangements I, II and III are 51.96, 53.97 and 47.14, respectively. The lower Nu in porous medium III is attributed to the less organized plume motion and less efficient vertical heat transfer.

5. Energy dissipation rates

RB convection is a closed system with exact balance properties. The overall kinetic and thermal energy dissipation rates $\epsilon_{u,T}$ are related to the governing and response parameters by two exact relations (Shraiman & Siggia 1990; Grossmann & Lohse 2000; Ahlers *et al.* 2009):

$$\langle \epsilon_u \rangle_{V,t} = \frac{\nu^3}{L^4} (Nu - 1) Ra Pr^{-2}, \quad \langle \epsilon_T \rangle_{V,t} = \kappa \frac{\Delta^2}{L^2} Nu, \quad (5.1)$$

where $\langle \cdot \rangle_{V,t}$ denotes the volume and time average, and

$$\epsilon_u = \frac{1}{2} \nu \sum_{ij} \left[\frac{\partial u_j}{\partial x_i} + \frac{\partial u_i}{\partial x_j} \right]^2, \quad \epsilon_T = \kappa \sum_i \left[\frac{\partial T}{\partial x_i} \right]^2. \quad (5.2)$$

We note that the exact global relations (5.1) are not affected by the presence of the obstacles. Figures 12 and 13 plot typical snapshots of the non-dimensional kinetic and thermal energy dissipation rates $\log_{10} \epsilon_{u,T}(\vec{x})$ on logarithmic scale for $Ra = 10^6, 10^8, 10^9$ and $\phi = 1, 0.92$. In the traditional RB convection with $\phi = 1$, it is found that the characteristic length scales of the flow structures become smaller for larger Ra , as shown in figures 12(*a - c*) and 13(*a - c*). A well-organized LSC develops at sufficiently large Ra , and velocity boundary layers appear close to both the horizontal plates and vertical sidewalls, which dominate the dissipation of kinetic energy. There are no thermal boundary layers along the sidewalls due to the imposed adiabatic condition for temperature, and the dissipation of thermal energy is dominated by plumes in the bulk and the thermal boundary layers near the horizontal top and bottom plates. The bulk contributions of both the kinetic and thermal energy dissipation rates are small (Grossmann & Lohse 2000, 2001, 2004; Zhang *et al.* 2017). Results of convection in a regular porous medium are displayed in figures 12(*d - f*) and 13(*d - f*). When Ra is small, convection is dominated by large-scale hot and cold plumes, penetrating to the top and bottom plates, respectively, along convection channels with fast velocities. Along these channels intense dissipation of kinetic energy occurs with length scale characterized by the pore scale. As Ra is increased, the length scales of the flow structures become smaller, and plumes wander in the bulk, leading to intense dissipation of kinetic energy in

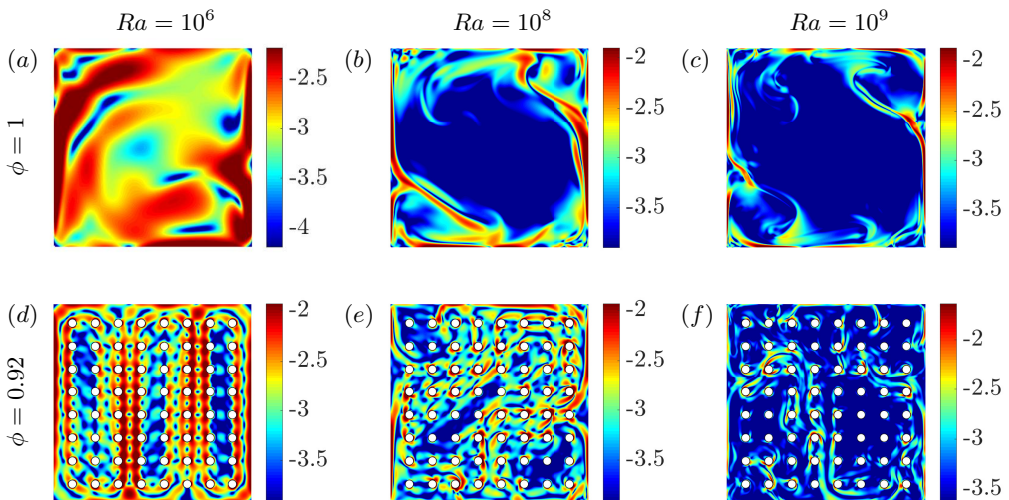


FIGURE 12. Typical snapshots of the kinetic energy dissipation rates $\log_{10}\epsilon_u(\vec{x})$ on logarithmic scale for different Ra and ϕ . $Ra = 10^6$, 10^8 , 10^9 for the figures in the left, middle, and right columns, respectively. (a – c) $\phi = 1$, (d – f) $\phi = 0.92$.

the bulk, in distinct contrast to the results of traditional RB convection with $\phi = 1$. For sufficiently large Ra , the kinetic energy dissipation in the bulk is concentrated around the obstacle surfaces due to the interaction between plumes and the obstacle array, and the pore scale is no longer a proper length scale for the kinetic energy dissipation. Due to the wandering motion of plumes in regular porous media, intense dissipation of thermal energy can occur locally in the bulk. However, the averaged bulk contribution of thermal energy dissipation remains small as compared to the boundary-layer contribution.

To further quantify the spatial distributions of the kinetic and thermal energy dissipation rates, we plot the profiles of averaged energy dissipation rates $\langle\epsilon_{u,T}\rangle_{x,t}$ along the vertical direction z in figure 15, showing the contributions of the bulk and boundary-layer regions. Using equations (5.1) Nu can be obtained by integrating these profiles of $\langle\epsilon_{u,T}\rangle_{x,t}$. Figure 15(a, b) plots the results of traditional RB convection with $\phi = 1$. The contributions of the boundary-layer region dominate for both the kinetic and thermal energy dissipation rates, consistent with the observations in figures 12 and 13. From figure 15(a) it seems to be less obvious that the kinetic energy dissipation is dominated by regions close to the walls. We note that $\langle\epsilon_u\rangle_{x,t}$ contains the kinetic energy dissipation from the velocity boundary layers near the sidewalls. Contrary to the velocity, the temperature field has no boundary layers close to the sidewalls, which are adiabatic. The results of convection in regular porous media are shown in figures 15(c, d). For these cases the obstacle array has a significant influence on the distribution of $\langle\epsilon_u\rangle_{x,t}$ due to the no-slip condition at the pores, while $\langle\epsilon_T\rangle_{x,t}$ is only mildly affected. The relative contribution of the bulk region of ϵ_u is significantly enhanced, while ϵ_T remains boundary-layer dominated. For relatively large Ra , intense dissipation of kinetic energy occurs around the obstacle surfaces. These observations are also consistent with those seen in figures 12 and 13.

In figure 2 it is shown that the heat transfer is enhanced when ϕ is slightly decreased from 1 at fixed Ra , and further decrease of ϕ reduces the heat transfer compared with the $\phi = 1$ case. To show the influence of the obstacle array on the heat transfer from

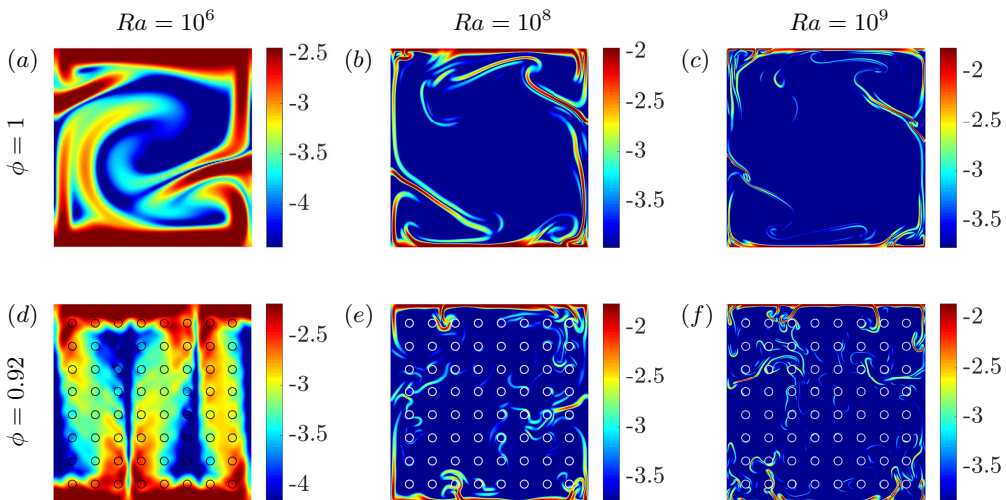


FIGURE 13. Typical snapshots of the thermal energy dissipation rates $\log_{10}\epsilon_T(\vec{x})$ on logarithmic scale for different Ra and ϕ . $Ra = 10^6$, 10^8 , 10^9 for the figures in the left, middle, and right columns, respectively. (a–c) $\phi = 1$, (d–f) $\phi = 0.92$. In (e) and (f), we show the obstacles as white thin circles. Note that the temperature field in them is well defined according to equation (2.2), and correspondingly the thermal energy dissipation rate $\epsilon_T(\vec{x}, t)$ is non-zero at these locations.

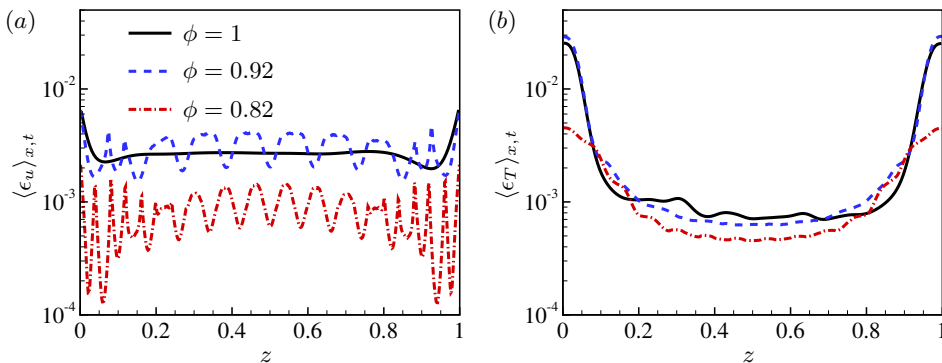


FIGURE 14. Variations of the averaged (a) kinetic and (b) thermal energy dissipation rates $\langle\epsilon_{u,T}\rangle_{x,t}$ with z for different ϕ at $Ra = 10^6$.

a local perspective, we plot the profiles of $\langle\epsilon_{u,T}\rangle_{x,t}$ for various ϕ at $Ra = 10^6$ in figure 14. As ϕ is slightly decreased from 1, the kinetic energy dissipation is enhanced in the bulk, which is the local manifestation of heat transfer enhancement due to the obstacle array. When ϕ is further decreased, the pore scale decreases accordingly and convection is significantly slowed down due to the drag of the obstacle array. Correspondingly, $\langle\epsilon_u\rangle_{x,t}$ is decreased in both the boundary-layer and the bulk regions, and $\langle\epsilon_T\rangle_{x,t}$ is also decreased, particularly in the boundary-layer region. Due to the smallness of the spatial coherence length and strong convection at large Ra , smaller porosity (or pore scale) is needed to significantly slow down the convection and reduce the overall energy dissipation rates.

For fixed ϕ , Nu increases with Ra with an effective power law $Nu \sim Ra^{0.65}$ when Ra is relatively small, and it changes to $Nu \sim Ra^{0.30}$ for large enough Ra . For

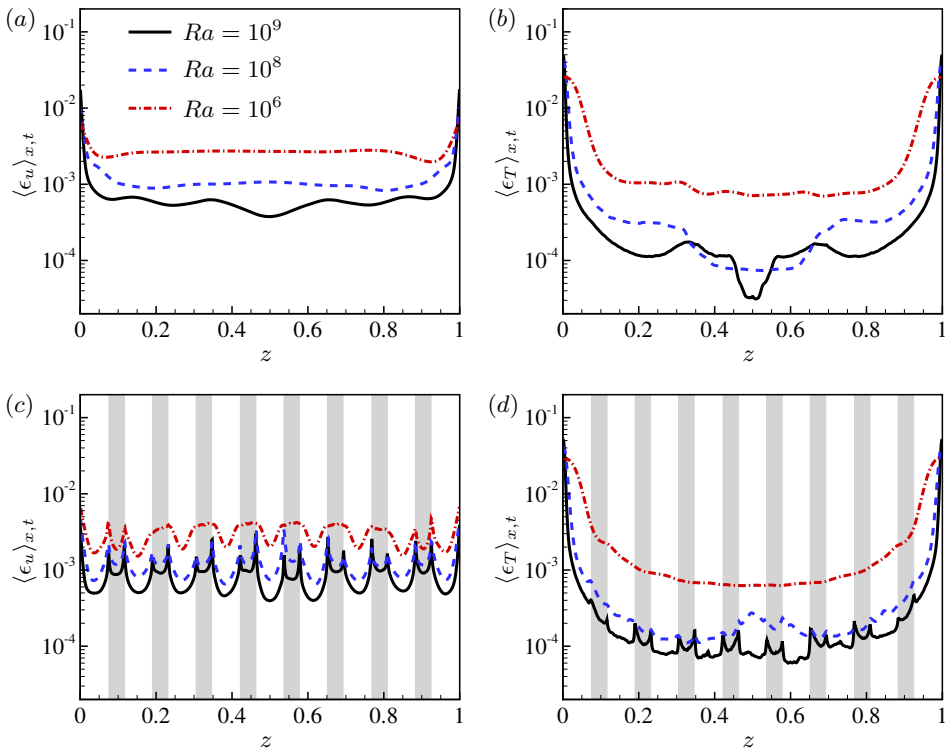


FIGURE 15. Variations of the averaged (a, c) kinetic and (b, d) thermal energy dissipation rates $\langle \epsilon_{u,T} \rangle_{x,t}$ with z for different Ra at (a, b) $\phi = 1$ and (c, d) $\phi = 0.92$. In (c, d) the grey areas indicate obstacle positions.

small Ra with the spatial coherence length larger than the pore scale, turbulence is suppressed in the pores. In the presence of the obstacle array one basically gets additional laminar-type boundary layers in the bulk region, namely, the laminar shear flows in the pores, and viscosity dominates such that the flow becomes of Prandtl-Blasius-Pohlhausen type. Intense dissipation of kinetic energy occurs along the convection channels. Thus, the overall kinetic energy dissipation rate can be estimated as $\langle \epsilon_u \rangle_{V,t} \sim \phi \nu U_{rms}^2 / l^2$, corresponding to the so-called ∞ -regime in Grossmann & Lohse (2001) for large Pr and small Ra , but with l replacing the box size L . Based on the exact relation between $\langle \epsilon_u \rangle_{V,t}$ and Nu , we can further estimate Nu as

$$Nu \approx c \cdot \phi \left(\frac{L}{l} \right)^4 Pr^2 Re^2 Ra^{-1} + 1, \quad (5.3)$$

where $Re = U_{rms} l / \nu$ and c is an undetermined constant (Grossmann & Lohse 2000, 2001, 2004). Plots of $Re(Ra)$ in the small- Ra regime are shown in figure 16(a) for four fixed ϕ , and then Nu can be estimated using equation (5.3). With $c = 8.0$, it is found that Nu obtained using equation (5.3) is consistent with the results based on the definition of Nu for different Ra and ϕ , as shown in figure 16(b), which provides additional confirmation of our observations regarding the modifications of the heat transfer and flow structure by the porous media. As Ra is increased, the characteristic scales of the flow structures become smaller and intense dissipation of kinetic energy tends to occur around the obstacle surfaces. For large enough Ra , convection in the pores becomes chaotic or even turbulent,

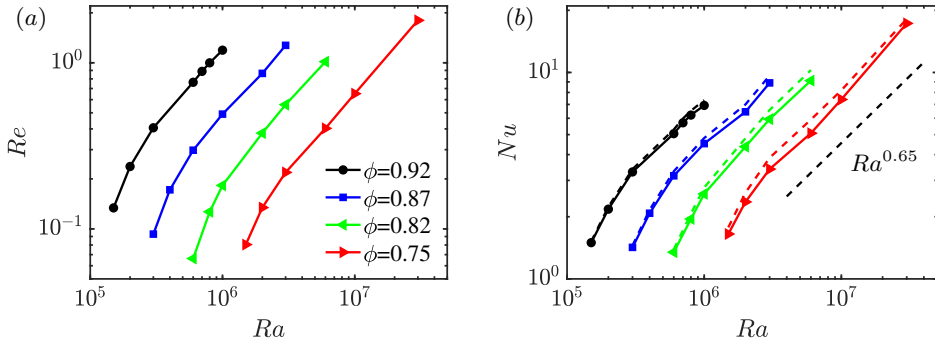


FIGURE 16. (a) $Re(Ra)$ in the small- Ra regime. (b) Comparison of Nu obtained based on the heat flux averaging $Nu = -\langle \partial_z T \rangle_{x,t}$ over the horizontal plates (dashed lines) and equation (5.3) with $c = 8.0$ (solid lines with symbols) for the same four cases for the porosity ϕ shown in (a).

the pore scale is no longer a proper length scale for the kinetic energy dissipation rate, and the estimate of Nu through equation (5.3) is no longer applicable.

6. Summary

We have studied the heat transfer and flow structure of 2D RB convection in regular porous media using pore-scale modeling. The porous medium is comprised of circular, solid obstacles located on a square lattice. The heat transfer between the fluid and solid phases is considered.

The obstacle array has two competing effects on the heat transfer. On the one hand, the flow becomes more coherent with the correlation between temperature fluctuation and vertical velocity enhanced and the counter-gradient convective heat transfer suppressed, leading to heat transfer enhancement. On the other hand, the convection strength is reduced due to the impedance of the obstacle array, leading to heat transfer reduction. The coexistence of the two competing effects leads to the non-monotonic behaviour of $Nu(\phi)$ as ϕ is decreased from 1, as shown in figure 2. The heat transfer enhancement is consistent with the counterintuitive observation that an appropriate strength of a stabilizing force can enhance heat transfer by increasing flow coherence (Chong *et al.* 2017). Significant enhancement of the heat transfer due to the increased flow coherence was also observed in the confined inclined convection in low- Pr fluids (Zwirner & Shishkina 2018). Due to the emergence of system-sized plume columns and the interaction of these plume columns with the opposed boundary layers in inclined convection, an increase of the heat transfer by a factor of approximately 2.3 can be realized. The observations of heat transfer enhancement in these distinct systems are manifestations of a universal mechanism to enhance turbulent transfer by increasing flow coherence.

The influence of porosity on flow properties is dependent on Ra , and two different heat transfer regimes are observed at fixed ϕ . In the small- Ra regime where viscosity dominates, Nu is decreased as compared to the $\phi = 1$ case with a steep effective power law $Nu \sim Ra^{0.65}$, while in the large- Ra regime Nu is increased as compared to $\phi = 1$ with the classical power law $Nu \sim Ra^{0.30}$. The scaling crossover occurs when the thickness of the thermal boundary layer δ_{th} is comparable to the pore scale l .

The influence of the obstacle array on the heat transfer is also analyzed from the local perspective, namely, the energy dissipation rates. It is found that the bulk contribution of kinetic energy dissipation rate is enhanced as ϕ is slightly decreased from 1; while when

ϕ is small enough, convection is significantly slowed down by the obstacle array, and the kinetic energy dissipation rate is decreased in the whole cell. For small Ra , due to the large coherence length of the flow structures and the impedance of the obstacle array, turbulence is suppressed in the pores and additional laminar-type boundary layers appear in the bulk. It is shown that also for porous-media convection Nu can be estimated from Re through equation (5.3) similarly to that suggested by Grossmann & Lohse (2001, 2004) for the viscosity-dominated so-called ∞ -regime. Regarding the turbulent modulations, the results of this study suggest that it is possible to modulate the heat transfer with porous structure and that the transitional Ra between different heat transfer regimes can be changed by manipulating the pore scale.

The influence of the obstacle arrangement on the flow structure is also studied. Three different arrangements with similar porosities are considered. The flow structure is found to be significantly influenced by the obstacle arrangement. In regular porous media, thermal plumes can penetrate deep into the bulk along convection channels aligning vertically, resulting in strong fluid and heat transport. When the obstacles are randomly located in the cell, the plume motion is less organized, and curved convection channels with strong flow emerge in the pores, with reduced efficiency of vertical heat transfer.

In this study we have mainly focused on the heat transfer and flow structure of 2D RB convection in regular porous media. In the future, it will be of interest to extend the study to the 3D case, to allow for a one-to-one comparison with experiment. Following the comparative study of Chong *et al.* (2017) and Lim *et al.* (2019), it is also desirable to investigate further turbulent flows with different stabilizing forces, to get an even more complete understanding of various stabilizing-destabilizing flow systems.

Acknowledgements

This work was supported by the Natural Science Foundation of China (Grant Nos. 11988102, 91852202, 11861131005 and 11672156), D.L.'s ERC-Advanced Grant (Grant No. 740479), and Tsinghua University Initiative Scientific Research Program (Grant No. 20193080058). Z.W. acknowledges the support of the Natural Science Foundation of China (Grant No. 11621202). S.L. acknowledges the project funded by the China Post-doctoral Science Foundation. We are grateful to the Dutch Supercomputing Consortium SURFsara and Chinese supercomputer Tianhe-2 for the allocation of computing time.

Declaration of interests

The authors report no conflict of interest.

REFERENCES

- AHLERS, G., GROSSMANN, S. & LOHSE, D. 2009 Heat transfer and large scale dynamics in turbulent Rayleigh-Bénard convection. *Rev. Mod. Phys.* **81** (2), 503–537.
- AMOOIE, M. A., SOLTANIAN, M. R. & MOORTGAT, J. 2018 Solutal convection in porous media: Comparison between boundary conditions of constant concentration and constant flux. *Phys. Rev. E* **98** (3), 033118.
- ARAÚJO, A. D., BASTOS, W. B., ANDRADE JR, J. S. & HERRMANN, H. J. 2006 Distribution of local fluxes in diluted porous media. *Phys. Rev. E* **74** (1), 010401.
- ARDEKANI, M. N., ABOUALI, O., PICANO, F. & BRANDT, L. 2018*a* Heat transfer in laminar Couette flow laden with rigid spherical particles. *J. Fluid Mech.* **834**, 308–334.
- ARDEKANI, M. N., AL ASMAR, L., PICANO, F. & BRANDT, L. 2018*b* Numerical study of heat transfer in laminar and turbulent pipe flow with finite-size spherical particles. *Int. J. Heat Fluid Fl.* **71**, 189–199.

- ATAEI-DADAVI, I., CHAKKINGAL, M., KENJERES, S., KLEIJN, C. R. & TUMMERS, M. J. 2019 Flow and heat transfer measurements in natural convection in coarse-grained porous media. *Int. J. Heat Mass Tran.* **130**, 575–584.
- BAO, Y., CHEN, J., LIU, B.-F., SHE, Z.-S., ZHANG, J. & ZHOU, Q. 2015 Enhanced heat transport in partitioned thermal convection. *J. Fluid Mech.* **784**, R5.
- BREUGEM, W.-P. 2012 A second-order accurate immersed boundary method for fully resolved simulations of particle-laden flows. *J. Comput. Phys.* **231** (13), 4469–4498.
- CHAKKINGAL, M., KENJEREŠ, S., ATA EI-DADAVI, I., TUMMERS, M. J. & KLEIJN, C. R. 2019 Numerical analysis of natural convection with conjugate heat transfer in coarse-grained porous media. *Int. J. Heat Fluid Fl.* **77**, 48–60.
- CHILLÀ, F. & SCHUMACHER, J. 2012 New perspectives in turbulent Rayleigh–Bénard convection. *Eur. Phys. J. E* **35** (7), 58.
- CHONG, K. L., HUANG, S.-D., KACZOROWSKI, M. & XIA, K.-Q. 2015 Condensation of coherent structures in turbulent flows. *Phys. Rev. Lett.* **115** (26), 264503.
- CHONG, K. L., WAGNER, S., KACZOROWSKI, M., SHISHKINA, O. & XIA, K.-Q. 2018 Effect of Prandtl number on heat transport enhancement in Rayleigh–Bénard convection under geometrical confinement. *Phys. Rev. Fluid* **3** (1), 013501.
- CHONG, K. L., YANG, Y.-T., HUANG, S.-D., ZHONG, J.-Q., STEVENS, R. J. A. M., VERZICCO, R., LOHSE, D. & XIA, K.-Q. 2017 Confined Rayleigh–Bénard, rotating Rayleigh–Bénard, and double diffusive convection: A unifying view on turbulent transport enhancement through coherent structure manipulation. *Phys. Rev. Lett.* **119** (6), 064501.
- CINAR, Y. & RIAZ, A. 2014 Carbon dioxide sequestration in saline formations: Part 2—Review of multiphase flow modeling. *J. Petrol. Sci. Eng.* **124**, 381–398.
- CINAR, Y., RIAZ, A. & TCHELEPI, H. A. 2009 Experimental study of CO₂ injection into saline formations. *SPE J.* **14**, 588–594.
- DE PAOLI, M., ZONTA, F. & SOLDATI, A. 2016 Influence of anisotropic permeability on convection in porous media: Implications for geological CO₂ sequestration. *Phys. Fluids* **28** (5), 056601.
- EMAMI-MEYBODI, H. & HASSANZADEH, H. 2015 Two-phase convective mixing under a buoyant plume of CO₂ in deep saline aquifers. *Adv. Water Resour.* **76**, 55–71.
- FADLUN, E. A., VERZICCO, R., ORLANDI, P. & MOHD-YUSOF, J. 2000 Combined immersed-boundary finite-difference methods for three-dimensional complex flow simulations. *J. Comput. Phys.* **161** (1), 35–60.
- GROSSMANN, S. & LOHSE, D. 2000 Scaling in thermal convection: A unifying theory. *J. Fluid Mech.* **407**, 27–56.
- GROSSMANN, S. & LOHSE, D. 2001 Thermal convection for large Prandtl numbers. *Phys. Rev. Lett.* **86** (15), 3316–3319.
- GROSSMANN, S. & LOHSE, D. 2004 Fluctuations in turbulent Rayleigh–Bénard convection: the role of plumes. *Phys. Fluids* **16** (12), 4462–4472.
- HASSANZADEH, H., POOLADIDARVISH, M. & KEITH, D. W. 2007 Scaling behavior of convective mixing, with application to geological storage of CO₂. *AIChE J.* **53** (5), 1121–1131.
- HEWITT, D. R., NEUFELD, J. A. & LISTER, J. R. 2012 Ultimate regime of high Rayleigh number convection in a porous medium. *Phys. Rev. Lett.* **108**, 224503.
- HEWITT, D. R., NEUFELD, J. A. & LISTER, J. R. 2014 High Rayleigh number convection in a three-dimensional porous medium. *J. Fluid Mech.* **748**, 879–895.
- HUANG, S.-D., KACZOROWSKI, M., NI, R. & XIA, K.-Q. 2013 Confinement-induced heat-transport enhancement in turbulent thermal convection. *Phys. Rev. Lett.* **111** (10), 104501.
- HUANG, Y.-X. & ZHOU, Q. 2013 Counter-gradient heat transport in two-dimensional turbulent Rayleigh–Bénard convection. *J. Fluid Mech.* **737**, R3.
- HUPPERT, H. E. & NEUFELD, J. A. 2014 The fluid mechanics of carbon dioxide sequestration. *Annu. Rev. Fluid Mech.* **46**, 255–272.
- JIANG, H.-C., ZHU, X.-J., MATHAI, V., VERZICCO, R., LOHSE, D. & SUN, C. 2018 Controlling heat transport and flow structures in thermal turbulence using ratchet surfaces. *Phys. Rev. Lett.* **120** (4), 044501.
- JIANG, L.-F., SUN, C. & CALZAVARINI, E. 2019 Robustness of heat transfer in confined inclined convection at high Prandtl number. *Phys. Rev. E* **99** (1), 013108.

- JOSEPH, D. D., NIELD, D. A. & PAPANICOLAOU, G. 1982 Nonlinear equation governing flow in a saturated porous medium. *Adv. Water Resour.* **18** (4), 1049–1052.
- KEENE, D. J. & GOLDSTEIN, R. J. 2015 Thermal convection in porous media at high Rayleigh numbers. *J. Heat Tran.* **137** (3), 034503.
- KEMPE, T. & FRÖHLICH, J. 2012 An improved immersed boundary method with direct forcing for the simulation of particle laden flows. *J. Comput. Phys.* **231** (9), 3663–3684.
- LAKKARAJU, R., STEVENS, R. J. A. M., ORESTA, P., VERZICCO, R., LOHSE, D. & PROSPERETTI, A. 2013 Heat transport in bubbling turbulent convection. *Proc. Natl Acad. Sci. USA* **110** (23), 9237–9242.
- LANDMAN, A. J. & SCHOTTING, R. J. 2007 Heat and brine transport in porous media: the Oberbeck-Boussinesq approximation revisited. *Transport in Porous Media* **70** (3), 355–373.
- LAPWOOD, E. R. 1948 Convection of a fluid in a porous medium. *Proc. Camb. Phil. Soc.* **44**, 508–521.
- LIM, Z.-L., CHONG, K. L., DING, G.-Y. & XIA, K.-Q. 2019 Quasistatic magnetoconvection: heat transport enhancement and boundary layer crossing. *J. Fluid Mech.* **870**, 519–542.
- LOHSE, D. & XIA, K.-Q. 2010 Small-scale properties of turbulent Rayleigh-Bénard convection. *Annu. Rev. Fluid Mech.* **42**, 335–364.
- NIELD, D. A. & BEJAN, A. 2006 *Convection in Porous Media*. Springer.
- NITHIARASU, P., SEETHARAMU, K. N. & SUNDARARAJAN, T. 1997 Natural convective heat transfer in a fluid saturated variable porosity medium. *Int. J. Heat Mass Tran.* **40** (16), 3955–3967.
- ORR, F. M. 2009 Onshore geologic storage of CO₂. *Science* **325** (5948), 1656–1658.
- OTERO, J., DONTCHEVA, L. A., JOHNSTON, H., WORTHING, R. A., KURGANOV, A., PETROVA, G. & DOERING, C. R. 2004 High-Rayleigh-number convection in a fluid-saturated porous layer. *J. Fluid Mech.* **500**, 263–281.
- VAN DER POEL, E. P., OSTILLA-MÓNICO, R., DONNERS, J. & VERZICCO, R. 2015 A pencil distributed finite difference code for strongly turbulent wall-bounded flows. *Comput. Fluids* **116**, 10–16.
- VAN DER POEL, E. P., STEVENS, R. J. A. M. & LOHSE, D. 2013 Comparison between two and three dimensional Rayleigh-Bénard convection. *J. Fluid Mech.* **736**, 177–194.
- RIAZ, A. & CINAR, Y. 2014 Carbon dioxide sequestration in saline formations: Part I—Review of the modeling of solubility trapping. *J. Petrol. Sci. Eng.* **124**, 367–380.
- SARDINA, G., BRANDT, L., BOFFETTA, G. & MAZZINO, A. 2018 Buoyancy-driven flow through a bed of solid particles produces a new form of Rayleigh-Taylor turbulence. *Phys. Rev. Lett.* **121** (22), 224501.
- SHISHKINA, O. & HORN, S. 2016 Thermal convection in inclined cylindrical containers. *J. Fluid Mech.* **790**, R3.
- SHISHKINA, O., STEVENS, R. J. A. M., GROSSMANN, S. & LOHSE, D. 2010 Boundary layer structure in turbulent thermal convection and its consequences for the required numerical resolution. *New J. Phys.* **12** (7), 075022.
- SHISHKINA, O. & WAGNER, C. 2011 Modelling the influence of wall roughness on heat transfer in thermal convection. *J. Fluid Mech.* **686**, 568–582.
- SHRAIMAN, B. I. & SIGGIA, E. D. 1990 Heat transport in high-Rayleigh-number convection. *Phys. Rev. A* **42** (6), 3650–3653.
- SOLTANIAN, M. R., AMOOIE, M. A., DAI, Z.-X., COLE, D. & MOORTGAT, J. 2016 Critical dynamics of gravito-convective mixing in geological carbon sequestration. *Sci. Rep.* **6**, 35921.
- SPANDAN, V., LOHSE, D., DE TULLIO, M. D. & VERZICCO, R. 2018 A fast moving least squares approximation with adaptive Lagrangian mesh refinement for large scale immersed boundary simulations. *J. Comput. Phys.* **375**, 228–239.
- SPANDAN, V., MESCHINI, V., OSTILLA-MÓNICO, R., LOHSE, D., QUERZOLI, G., DE TULLIO, M. D. & VERZICCO, R. 2017 A parallel interaction potential approach coupled with the immersed boundary method for fully resolved simulations of deformable interfaces and membranes. *J. Comput. Phys.* **348**, 567–590.
- STEVENS, R. J. A. M., LOHSE, D. & VERZICCO, R. 2014 Sidewall effects in Rayleigh-Bénard convection. *J. Fluid Mech.* **741**, 1–27.

- STEVENS, R. J. A. M., VERZICCO, R. & LOHSE, D. 2010 Radial boundary layer structure and Nusselt number in Rayleigh–Bénard convection. *J. Fluid Mech.* **643**, 495–507.
- STEVENS, R. J. A. M., ZHONG, J.-Q., CLERCX, H. J. H., AHLERS, G. & LOHSE, D. 2009 Transitions between turbulent states in rotating Rayleigh–Bénard convection. *Phys. Rev. Lett.* **103** (2), 024503.
- SUGIYAMA, K., NI, R., STEVENS, R. J. A. M., CHAN, T. S., ZHOU, S.-Q., XI, H.-D., SUN, C., GROSSMANN, S., XIA, K.-Q. & LOHSE, D. 2010 Flow reversals in thermally driven turbulence. *Phys. Rev. Lett.* **105** (3), 034503.
- DE TULLIO, M. D. & PASCAZIO, G. 2016 A moving-least-squares immersed boundary method for simulating the fluid–structure interaction of elastic bodies with arbitrary thickness. *J. Comput. Phys.* **325**, 201–225.
- UHLMANN, M. 2005 An immersed boundary method with direct forcing for the simulation of particulate flows. *J. Comput. Phys.* **209** (2), 448–476.
- VANELLA, M. & BALARAS, E. 2009 Short note: A moving-least-squares reconstruction for embedded-boundary formulations. *J. Comput. Phys.* **228** (18), 6617–6628.
- VERZICCO, R. 2002 Sidewall finite-conductivity effects in confined turbulent thermal convection. *J. Fluid Mech.* **473**, 201–210.
- VERZICCO, R. 2004 Effects of nonperfect thermal sources in turbulent thermal convection. *Phys. Fluids* **16** (6), 1965–1979.
- WAGNER, S. & SHISHKINA, O. 2015 Heat flux enhancement by regular surface roughness in turbulent thermal convection. *J. Fluid Mech.* **763**, 109–135.
- WANG, Q., WAN, Z.-H., YAN, R. & SUN, D.-J. 2018 Multiple states and heat transfer in two-dimensional tilted convection with large aspect ratios. *Phys. Rev. Fluids* **3** (11), 113503.
- WANG, Z.-Q., MATHAI, V. & SUN, C. 2019 Self-sustained biphasic catalytic particle turbulence. *Nat. Commun.* **10** (1), 3333.
- WEN, B.-L., CORSON, L. T. & CHINI, G. P. 2015 Structure and stability of steady porous medium convection at large Rayleigh number. *J. Fluid Mech.* **772**, 197–224.
- WOODING, R. A. 1957 Steady state free thermal convection of liquid in a saturated permeable medium. *J. Fluid Mech.* **2** (3), 273–285.
- XIA, K.-Q. 2013 Current trends and future directions in turbulent thermal convection. *Theor. App. Mech. Lett.* **3** (5), 052001.
- YANG, Y.-T., VAN DER POEL, E. P., OSTILLA-MÓNICO, R., SUN, C., VERZICCO, R., GROSSMANN, S. & LOHSE, D. 2015 Salinity transfer in bounded double diffusive convection. *J. Fluid Mech.* **768**, 476–491.
- YANG, Y.-T., VERZICCO, R. & LOHSE, D. 2016 Scaling laws and flow structures of double diffusive convection in the finger regime. *J. Fluid Mech.* **802**, 667–689.
- ZHANG, Y., ZHOU, Q. & SUN, C. 2017 Statistics of kinetic and thermal energy dissipation rates in two-dimensional turbulent Rayleigh–Bénard convection. *J. Fluid Mech.* **814**, 165–184.
- ZHONG, J.-Q., STEVENS, R. J. A. M., CLERCX, H. J. H., VERZICCO, R., LOHSE, D. & AHLERS, G. 2009 Prandtl-, Rayleigh-, and Rossby-number dependence of heat transport in turbulent rotating Rayleigh–Bénard convection. *Phys. Rev. Lett.* **102** (4), 044502.
- ZHU, X.-J., STEVENS, R. J. A. M., SHISHKINA, O., VERZICCO, R. & LOHSE, D. 2019 $Nu \sim Ra^{1/2}$ scaling enabled by multiscale wall roughness in Rayleigh–Bénard turbulence. *J. Fluid Mech.* **869**, R4.
- ZHU, X.-J., STEVENS, R. J. A. M., VERZICCO, R. & LOHSE, D. 2017 Roughness-facilitated local $1/2$ scaling does not imply the onset of the ultimate regime of thermal convection. *Phys. Rev. Lett.* **119** (15), 154501.
- ZWIRNER, L. & SHISHKINA, O. 2018 Confined inclined thermal convection in low-Prandtl-number fluids. *J. Fluid Mech.* **850**, 984–1008.